ADVANCED MATERIALS INTERFACES
www.advmatinterfaces.de

Nucleation Behavior of SnS_2 on Thiol Functionalized SAMs During Solution-Based Atomic Layer Deposition

Klaus Götz, Annemarie Prihoda, Chen Shen, Martin Dierner, Johannes Dallmann, Saskia Prusch, Dirk Zahn, Erdmann Spiecker, and Tobias Unruh**

Solution-based atomic layer deposition (sALD) is an emerging technique that transfers the principle of traditional atomic layer deposition (ALD) from the gas phase into a wet chemical environment. This new preparation technique has new and unique properties and requirements. A large number of new surfaces and reactants are available to produce active 2D materials.
In this work a reproducible procedure to coat silicon wafers with a densely packed monolayer of (3-Mercaptopropyl)trimethoxysilane (MPTMS) molecules is presented. These highly functionalized surfaces can be used to seed the nucleation of SnS_2 in a solution-based ALD procedure. A coating routine for the production of SnS_2 is adapted from ALD to sALD and insight into the nucleation behavior of the reactands is given. X-ray reflectometry (XRR) is used to resolve the nucleation process of SnS_2 on an MPTMS self assembled monolayer (SAM) during the first three cycles of an sALD procedure. The comparison of ex situ XRR, in situ XRR, grazing incidence wide-angle X-ray scattering (GIWAXS), atomic force microscopy (AFM), energy dispersive X-ray spectroscopy (EDX) measurements, and density functional theory (DFT) calculations find that SnS_2 first forms a closed layer and then continues to grow in islands on thiol functionalized silane SAMs. Subsequent coating cycles will continue the growth of the islands laterally and in height.

1. Introduction

Since the discovery of the electronic properties of graphene[1] 2D materials have been the topic of extensive studies for their use in functional devices.[2–5] The quality, i.e. crystallinity, exact dimensions, and purity of these materials play an important role in the efficiency of the devices.[6–8]

A well established technique to produce 2D materials that are defined on an atomic level is atomic layer deposition (ALD). It allows a homogeneous coating of 3D structured surfaces with a 2D material with atomic precision. This technique is based on a cyclical procedure of self-limiting chemical reactions of two precursors. In two separate steps, an active surface is dosed with one of the precursors. The active sites react only with one of the precursors, such that the chemical reaction, and therefore the coating step, ends when all active sites have reacted with the respective precursor. The first precursor in turn needs to create new active sites for the second precursor and vice versa. In this way, atomically defined layers of active material can be created. Traditional ALD, however, comes with challenges. The method is performed in a vacuum by dosing the surface with precursors in gas phase, which limits the choice of precursors and makes large scale production very costly.[9–11] Nevertheless, ALD has been suc-

---

K. Götz, A. Prihoda, J. Dallmann, T. Unruh
Friedrich-Alexander-Universität Erlangen-Nürnberg (FAU)
Institute for Crystallography and Structural Physics (ICSP)
Staudtstr. 3, 91058 Erlangen, Germany
E-mail: klaus.klagoe.goetz@fau.de; Tobias.Unruh@fau.de

K. Götz, A. Prihoda, M. Dierner, E. Spiecker, T. Unruh
Friedrich-Alexander-Universität Erlangen-Nürnberg (FAU)
Center for Nanoanalysis and Electron Microscopy (CENEM)
Cauerstr. 3, 91058 Erlangen, Germany

The ORCID identification number(s) for the author(s) of this article can be found under https://doi.org/10.1002/admi.202300990

DOI: 10.1002/admi.202300990

K. Götz, A. Prihoda, M. Dierner, E. Spiecker, T. Unruh
Friedrich-Alexander-Universität Erlangen-Nürnberg (FAU)
Interdisciplinary Center for Nanostructured Films (IZNF)
Cauerstr. 3, 91058 Erlangen, Germany

C. Shen
Deutsches Elektronen-Synchrotron DESY
Notkestr. 85, 22607 Hamburg, Germany

M. Dierner, E. Spiecker
Friedrich-Alexander-Universität Erlangen-Nürnberg (FAU)
Lehrstuhl für Mikro- und Nanostrukturforschung (IMN)
Cauerstr. 3, 91058 Erlangen, Germany

S. Prusch, D. Zahn
Friedrich-Alexander-Universität Erlangen-Nürnberg (FAU)
Lehrstuhl für Theoretische Chemie, Computer-Chemie-Centrum, Department of Chemistry and Pharmacy(DCP)
Nägelsbachstr. 25, 91052 Erlangen, Germany

cessfully used to create active materials for a wide range of functional devices.[12–15]

Solution-based ALD (sALD) is an emerging technique that circumvents these challenges and opens up new possibilities. This method aims to keep the basic principle of alternating, self-limiting reactions to create atomically well defined active layers. In contrast to ALD, sALD is performed in a wet chemical environment instead of a vacuum. This approach has two main advantages. First, without the need of vacuum evaporation a wider range of precursors can be utilized. Second, the use of a wet chemical environment together with automated pump systems and reactors enables an easier approach to up-scaling. Therefore sALD is a step toward the creation of printable active systems. In recent years sALD has already been successfully used to create atomic layers of SnS_2 and HfS_2.[16–19]

In recent years SnS_2 has been investigated for its potential in photocatalytic splitting of water.[20–23] It is a non-toxic material with a bandgap in the range between 2.52 and 2.8 eV, which can be tuned by material thickness.[24] Recently Hu et al.[25] found, that amorphous SnS_2 layers prepared by ALD significantly enhanced the photocatalytic efficiency of the material. Additionally, from chemical vapor deposition (CVD) studies it is known that different surface conditions such as surface roughness, oxidation state, and the availability of functional groups can drastically alter the nucleation process of 2D materials and therefore the properties of the resulting layers.[26,27] Therefore, a good understanding of the underlying principles of the technique is crucial in optimizing the process and tuning of the final product.

This work focuses on X-ray reflectometry (XRR) as a fast and non-destructive tool for the ex situ and in situ characterization of single atomic layers. Our previous work shows that XRR is a technique well suited to investigate interface layers of only a few Å in thickness.[28–31] Using the brilliant X-ray sources at the P08 beamline at DESY, XRR measurements have been performed in situ to investigate the nucleation process during the first few cycles of an sALD procedure.

This work presents our results on the nucleation process of SnS_2 on active surfaces created by a self assembled monolayer (SAM) of (3-Mercaptopropyl)trimethoxysilane (MPTMS) on silicon wafers.

2. Results and Discussion

2.1. Characterization of the MPTMS SAM

It is crucial to develop a reliable and reproducible procedure for the formation of stable SAMs to be used as a model system and as well-suited, functionalized supports for sALD coatings. These systems have to be thoroughly pre-characterized to give a clear picture of the structure of the SAMs. We characterized the SAMs using contact angle measurement, atomic force microscopy (AFM), and XRR to examine wettability, topography, packing density, layer thickness, and the electron density profile (EDP) of the layer perpendicular to the substrate surface. Representative results for an MPTMS SAM preparation are displayed in **Figure 1** The statistical evaluation of 14 MPTMS SAMs is presented in the Supporting Information.

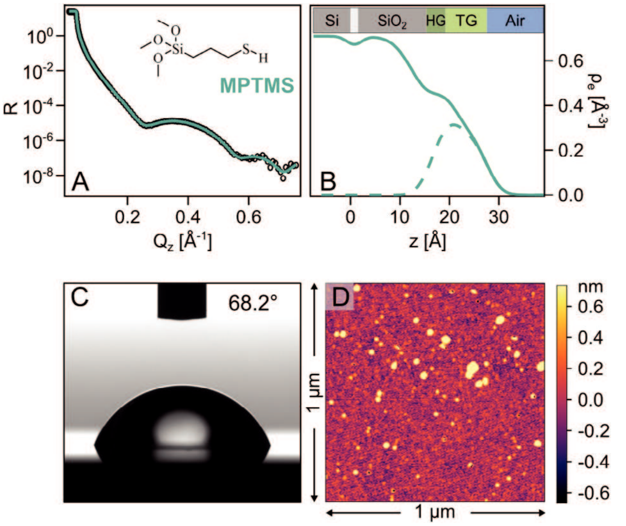

Figure 1. Characterization of an MPTMS SAM on a silicon substrate. A) Reflectivity data (circles), fit (solid line), and structure formula of the MPTMS molecule. B) Corresponding EDP (solid line) and EDP of the MPTMS SAM without substrate contribution (dashed line). A depleted electron density layer based on the model of Steinrück et al.[32] is between silicon and native silicon dioxide. HG = Head group, TG = Tail group. C) Water contact angle. D) AFM image.

Figure 1A,B show the XRR curve and corresponding EDP of an MPTMS SAM. The SAM layer thickness of $d \approx 12.2 \pm 1.9$ Å ($d_{chain} \approx 8.8$ Å for the carbon chain and $d_{head} \approx 3.4$ Å for the head group) and the surface root-mean-square(rms)-roughness of 2.3 Å leads to a slight bump in the EDP at $z = 20$ Å. Rebiscoul et al.[33] reported a similar film thickness (≈10 Å) for a monolayer. The discrepancy between the measured chain length and the calculated projected chain length (4.1 Å) can be explained by a disorder in the bonding region. If not all three methoxy groups of the molecule bind covalently to the substrate, the unbound methoxy groups can react with other MPTMS molecules and form intermolecular siloxane bonds. Consequently, these additional molecules are not directly bound to the substrate surface, but indirectly via an already bound MPTMS molecule. This may result in an extended head group region, which results in an increased SAM layer thickness. This leads to an extended chain length of the fit, since the thickness of the head group was kept constant. Such a molecular arrangement leads to a less densely packed layer, which is confirmed by the overall electron density of the SAM (0.25 ± 0.07 Å^{-3}) and by the corresponding low packing density of 71% as determined from the XRR data analysis. The packing density is calculated by taking the ratio of the measured chain electron density and the theoretical chain electron density (0.346 Å^{-3}), which is based on the mass density of the liquid phase of bulk MPTMS.[34] The reduced packing density gives some spatial freedom to the MPTMS molecules in the SAM, such that they are not strictly oriented perpendicular to the substrate and some thiol groups are probably not located directly at the solid–air interface.

The surface roughness of the SAM is 2.3 Å, which is in reasonable agreement with the rms-roughness of 3.5 Å determined by an AFM measurement (cf. Figure 1D). The bumps visible in the AFM image (yellow spots) can most likely be attributed to MPTMS polymer formation.[35] Since these areas cover less than

2% of the surface and in XRR the beam averages over a large area, we do not expect this to significantly affect the results that are extracted here from the XRR data.

The mean contact angle of water against the solid supported SAM averaged over six different positions on the sample was found to be 68.0° ± 0.8°. An example of a contact angle measurement is visualized in Figure 1C. Literature values for water contact angles on MPTMS SAMs vary considerably between 35° and 78°.[36–39] From this variation, it is evident that there can be significant differences in the contact angle and thus in the quality of the coatings, due to the coating method and the chemicals used.

2.2. Density Functional Theory (DFT) Calculations of Fundamental Reaction Steps

To characterize the very initial processes determining the first half cycle of the sALD procedure, we performed a small series of DFT calculations to explore the energetics of reactions (2,3) as discussed in section 4 (using R = C_3H_7). For this, the thiol-functionalized SAM was approximated by a C_3H_7SH moiety and reaction (2) was considered as a) the association of a tetrakis(dimethylamido)tin (IV) (TDMASn) precursor, followed by b) S–Sn bond formation and $(CH_3)_2NH$ dissociation. The overall reaction energy in the gas phase (a+b) was found as −0.70 eV. In turn, TDMASn association to C_3H_7SH via hydrogen bonds (a) showed a local energy minimum arrangement giving rise to −0.32 eV formation energy. On this basis, we suggest that the thiolated SAM reacts with the TDMASn precursors in a twofold manner, namely by establishing S–Sn bonds as far as sterically possible, whilst more remote thiols may further stabilize precursor association by hydrogen bonds.

Next, the second step of the first half cycle was investigated. For this, the covalently bound precursor setup of the beforehand discussed reaction (2) was taken as a $[(CH_3)_2N]_3\ [C_3H_7S]Sn$ species reacting with $3 \cdot H_2S$. On this basis, the energy of reaction (3) was found as −1.82 eV in the gas phase. The energy change per $[SH]^-$ thus reads −0.61 eV – as compared to the −0.70 eV energy gain of reaction (2). This suggests the stability of precursor binding to the thiolated SAM during the second step of the first half cycle.

However, the picture gets increasingly complex upon implementing further sALD cylces. Indeed, it is intuitive to expect S–Sn bonds in bulk SnS_2 (thus formally involving S^{2-} species) to outperform the SAM-precursor interactions. We argue that the fate of the SAM-SnS_2 interface therefore critically depends on how gradual structures evolve during the first 3 sALD cycles as discussed in the following.

2.3. In Situ sALD Study

2.3.1. Synchrotron XRR Measurements

Initially, the MPTMS coated wafers were measured by XRR in the flow cell filled with pure tetrahydrofuran (THF). Subsequently, XRR patterns were collected following each half cycle of the sALD procedure. These measurements were also performed in the flow cell filled with THF. The XRR data are displayed in **Figure** 2a. As a main feature, a distinct interference minimum is observed at 0.6 Å $^{-1}$ which shifts toward 0.5 Å $^{-1}$ upon contact with the tin precursor and gradually shifts further with each half cycle, and ends at 0.45 Å $^{-1}$ after 3 sALD cycles. This decrease in the minimum position can be attributed to a growing layer on top of the SAM.

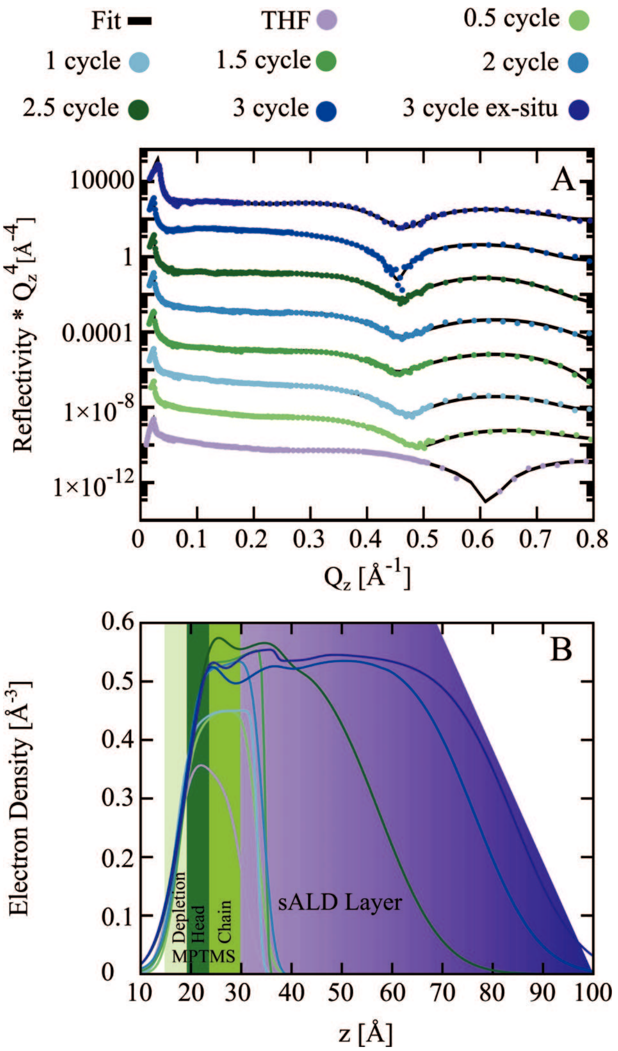

Figure 2. Reflectivity data of MPTMS coated silicon wafer during the first 3 cycles of SnS_2 sALD coating. A) experimental reflectivity data (circles) of the initial MPTMS layer and after each half cycle of the coating procedure in THF as well as a final measurement ex situ in helium. The black lines indicate the reflectivity curve of the fitted models. The data sets were shifted vertically for better visualization. B) EDDPs of the MPTMS and sALD layers of the fit model. Colored areas indicate the contributions in the fit model.

The data was subsequently fitted with the model described in section 4. The electron density difference profiles (EDDPs) are displayed in Figure 2b. They were used to calculate the electron density and thickness of the combined layers. The data was numerically integrated using the Simpson algorithmm of the Python module scipy.integrate.[40] This area was then divided by the full width half maximum of the EDDP to calculate the electron density. Furthermore the electron density of a 1.3 nm thick surface layer was calculated for comparison with the AFM results. For the samples with a low surface roughness (MPTMS, 0.5, 1.0, 1.5, and 2.0 cycles) the location of the

Table 1. Thickness and maximal electron density of the total coating consisting of MPTMS SAM and sALD layer. The growth of the sALD layer was calculated as $\Delta d_{\mathrm{total,\,i}} = d_{\mathrm{total,\,i}} - d_{\mathrm{total,\,i\,-\,0.5}}$, with i denoting the respective cycle number. ρ_{surf} denotes the electron density in the top 1.3 nm of the combined layer. The roughness of the combined is given as σ.

Cycles	d_{total} [Å]	$\Delta d_{\mathrm{total}}$ [Å]	ρ_e [Å $^{-3}$]	Γ_e	ρ_{surf} [Å $^{-3}$]	Γ_{surf}	σ [Å]
ine							
0	13.5	n.a.	0.36	n.a.	0.18	n.a.	7.72
0.5	15.5	2.0	0.45	0.368	0.29	0.238	1.89
1	16.0	0.5	0.45	0.374	0.38	0.314	1.30
1.5	16.5	0.5	0.54	0.446	0.49	0.402	5.05
2	16.0	−0.5	0.55	0.451	0.37	0.304	1.85
2.5	38.0	22.0	0.58	0.478	0.28	0.234	9.99
3	59.0	21.0	0.53	0.437	0.26	0.216	10.00
3 ex situ	65.0	6.0	0.55	0.452	0.27	0.225	10.00

surface was identified by the z value at which the EDDP falls below 1 % of its maximum value. For the EDDPs displaying a high surface roughness the center of the surface was identified with the z-value where the EDDP reaches half of its maximum value. The EDDPs and integrated areas are displayed separately in Figure S2 (Supporting Information) the results are listed in **Table 1**.

The MPTMS SAM is visible in the initial measurement against THF with a thickness of 13.5 Å and an electron density of 0.36 Å $^{-3}$. This corresponds to a closely packed MPTMS layer. From the fits to the XRR data of the pure MPTMS layer a mean area of 21.8 Å ^{2} per MPTMS molecule could be determined. This leads to a mean distance of 5.0 Å between the molecules assuming an idealized model of a regularly hexagonally closest packed structure.

For z-values larger than 50 Å a large diffuse layer is visible in all EDPs after the first half cycle. The exact size of this layer cannot be determined accurately, since an increase of the layer thickness above 50 Å would not alter the intensity of the reflectivity curve significantly at any scattering angle. Nevertheless, there is a trend toward an increasing electron density of this layer from 0.4 to 0.55 Å $^{-3}$, showing that material is deposited during the cycles.

After the first half cycle of TDMASn the combined layer of MPTMS and the sALD product grows by 2 Å and the electron density increases from 0.36 to 0.45 Å $^{-3}$. After the subsequent half cycle of H_2S the electron density of the combined layer does not change significantly, whereas the thickness increases by 0.5 Å. The roughness of the layer however is decreased leading to a smoother interface.

From these results we can already determine an electron surface density. Assuming the number of MPTMS molecules on the surface does not change, the increase of electrons per MPTMS molecule can be calculated. Initially there were 106 e$^-$ per 21.81 Å ^{2} (the area occupied by one MPTMS molecule). After the first TDMASn cycle we find 152.13 e$^-$ on the same surface area, which gives an additional 46.13 electrons per MPTMS molecule. Comparing this with the 46 electrons of a Sn(IV) ion of the TDMASn precursor shows, that statistically all thiol groups reacted with one precursor molecule. The fact that the electron density of the MPTMS layer is increasing together with the sALD layers can be interpreted such that material is growing not only on top of the MPMTS layer but also incorporated into it.

The electron density of the remaining dimethylamine groups of TDMASn does not contribute to this calculation as it is not visible in the EDDP. In contrast to the Sn(IV) ions, which mostly form a confined layer of atoms with a high number of electrons, the dimethylamine groups have a low electron density, are spread over a larger area, and point toward the dispersion medium. Because of the good solubility in THF we expect no depletion layer between the dimethylamine groups and THF and therefore only minimal contrast. The diffuse layer however produces a high contrast in the region where we would expect the dimethylamine groups, therefore making it impossible to accurately discern their contribution.

After the second half cycle with TDMASn, the electron density of the combined layer increases to 0.54 Å $^{-3}$ and the thickness grows by 1 Å. From the second half cycle of H_2S a change of neither the electron density nor the thickness of the layer could be determined and only the surface roughness increased slightly. The third half cycle of TDMASn leads to a slight increase in electron density to 0.58 Å $^{-3}$ and a growth of the thickness of the combined layer by 22 Å. The layer roughness increases from values <2 Å to 10 Å. After the third half cycle of H_2S the layer growths by another 21 Å and the overall electron density decreases slightly to 0.53 Å $^{-3}$. After removing the wafer from the flow cell and drying it the layer thickness is increased by 6 Å.

The continued increase of the combined layer's electron density and simultaneous stagnation of its growth during the first two cycles, shows that the sALD material is incorporated in the already existing layer instead of forming a new sALD layer. This can be interpreted as the material growing in islands on the surface and progressively filling the gaps between the material with each continued cycle. For the first two cycles, a slow growth of sALD material on top of the MPTMS layer is observed. The growth rate of 2 and 1 Å cycle^{-1} coincides well with the results from the literature, e.g., SnS_2 (0.84 Å −1.33 Å cycle^{-1}).[13] TiO_2 (0.3 Å cycle^{-1}),[41] PbS (1.2 Å −1.7 Å cycle^{-1}),[18] or MgO (1 Å cycle^{-1})[41] With each cycle the diffuse layer grows because of an accumulation of free precursor molecules that were not removed during the cleaning procedure. After the second cycle this accumulation becomes so extended, that the sALD layer can not be distinguished from the diffuse layer anymore.

The same behavior could be observed in preliminary ex situ investigations detailed in Section 6 (Supporting Information).

The electron density of crystalline berndtite SnS_2 is $\rho_{\mathrm{berndtite}} = 1.22$ Å $^{-3}$.[42] Assuming a similar electron density in the deposited material the surface coverage after each cycle $\Gamma_{\mathrm{e,\,i}}$ (i: cycle number) can be calculated from the electron density $\rho_{\mathrm{e,\,i}}$ as:

$$\Gamma_{\mathrm{e,i}} = \frac{\rho_{\mathrm{e,i}}}{\rho_{\mathrm{berndtite}}} \tag{1}$$

with $\Gamma_1 = 0.374$, $\Gamma_2 = 0.451$, and $\Gamma_3 = 0.437$.

2.3.2. Post-Characterizations

The samples produced during the in situ measurements at P08 were further characterized after the beamtime. The samples were

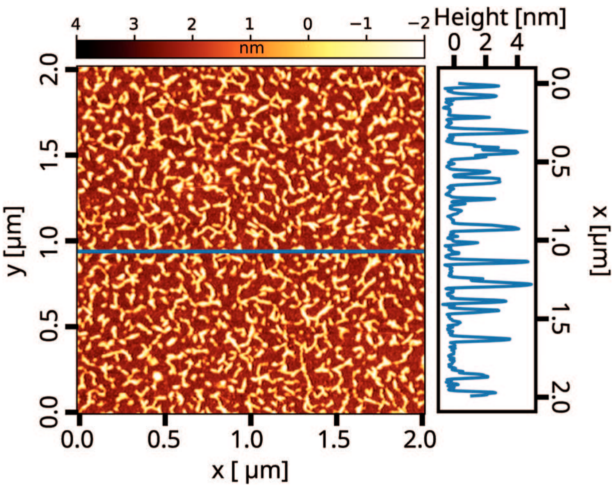

Figure 3. AFM image of the in situ sample. The sample was cleaned by ultrasonicating for 1h in THF. The worm like structures, corresponding to SnS_2 islands can be observed. These structures are typical for the sALD process described here. They cover roughly a third of the available surface. The right plot shows a height cross section along the blue line indicated in the AFM picture.

cleaned by submerging them in THF in an ultrasonic bath for 1 h. The cleaned samples were investigated using AFM, grazing incidence wide-angle X-ray scattering (GIWAXS), and energy dispersive X-ray spectroscopy (EDX). The EDX measurements confirmed the presence of nanosized structures and the presence of tin and sulfur. The images and spectra are shown in Figure S4 (Supporting Information). The small amount of SnS_2 in the thin layer did however not allow a quantitative analysis of the amount of Sn and S in the sALD layer.

2.3.3. AFM

AFM pictures were taken at multiple, random positions on the sample. In these pictures, large microstructures are visible all over the sample even after a rigorous cleaning procedure. Large areas are however clear of these structures and show the surface structure of material deposited by sALD. One exemplary picture is shown in **Figure** 3. The image shows the island growth of the material in the form of worm-like structures. These structures have heights between 2 and 4 nm, widths of ≈20 nm, and lengths of up to 250 nm. Averaging over these areas gives a root-mean-square roughness of the surface of 1.3 nm. A grain analysis of the images, counting areas that elevate more than 1 nm gives a surface coverage of ≈33% with these worm -like structures.

Similar worm-like shaped islands have been reported by Zhang et al.[27] for the growth of SnS_2 on SiO_2/Si by chemical vapor deposition (CVD). They observed SnS_2 structures of comparable length and width for CVD dosing times of 30 s, albeit with a lesser surface coverage. It is proposed that at first deposited SnS_2 forms amorphous nucleation seeds that grow unstructured. At a certain critical size of ≈3 – 4 nm, the nuclei start to exhibit a berndtite crystal structure with a preferred growth direction along the surface of the SiO_2/Si wafer. The layer only starts growing perpendicular to the surface when this nucleation layer is completely filled with growth centers.

2.3.4. GIWAXS

GIWAXS measurements were performed at a sample detector distance of 168 mm. The two dimensional detector image is visualized in **Figure** 4A. The scattering signal is radially homogeneous indicating no preferential orientation of the nanostructures on the surface. The radially averaged data is displayed in Figure 4B. It consists of two main contributions: The feature in the *Q*-range between 0.2 and 0.8 Å $^{-1}$ is the small angle signal and arises from the form factor of the nanostructures. The peak ≈2 Å $^{-1}$ can be attributed to the internal atomic structure of the deposited material.

The GIWAXS data was fitted using the DISCUS software suite.[43] The nanostructures observed by AFM inspired the fit model. In this model, the system is approximated by ellipsoidal berndtite nanocrystals. The scattering signal of the nanoparticle structures was calculated from an ellipsoidal arrangement of Sn and S atoms. These arrangements were produced by simulating a large berndtite crystal measuring 20 unit cells in every lattice dimension with DISCUS and finally cutting an ellipsoidal shape from this block. Fitting parameters were the lengths of the principal semi-axes and the position of the center of the ellipsoid relative to the origin of the unit cell. The fit resulted in ellipsoidal nanoparticles with principal semi axes of 23.7 and 68.9 Å in accordance to the structures observed in AFM. The fit model reproduces the small angle part of the GIWAXS data and describes the scattering qualitatively as well at larger Q values especially the peak at ≈2.2 Å $^{-1}$. The model does not take into account surface restructuring of the deposited material, bulk and surface strain or possible secondary phases which could explain the differences in the model and measured data.

2.3.5. Growth Behavior

Ex situ (c.f. Supporting Information) and in situ XRR experiments showed, that during the first few cycles of sALD of SnS_2 on MPTMS coated Si wafers, SnS_2 is incorporated into the MPTMS layer. During the first cycle an almost complete sALD reaction at the functional thiol groups of the MPTMS molecules is observed. However, from the density of the MPTMS layer with an average molecular distance of 5.0 Å it is obvious that a complete SnS_2 layer, especially a crystalline SnS_2 layer, can not be achieved. Rather a compaction of the initial layer followed by the growth of islands follows this initial layer formation upon the next sALD cycles.

Accordingly, the second cycle shows no vertical growth of the layer but an increase of the electron density of the initial layer. This suggests, that instead of forming a second layer the Sn atoms from the second TDMASn cycle are integrated into the space between the previously deposited Sn atoms and interconnected by the S atoms from the H_2S cycle. Thus a closed, but still amorphous, layer of SnS_2 is formed on top of the MPTMS SAM.

DFT calculations support the possibility of the growth of islands in the later steps, as the layer growth has to compete with the restructuring of the deposited material to form crystalline SnS_2. Such a process could lead to the observed nanostructures.

From AFM and GIWAXS measurements it could be concluded that on top of this closed SnS_2 layer, SnS_2 islands are formed

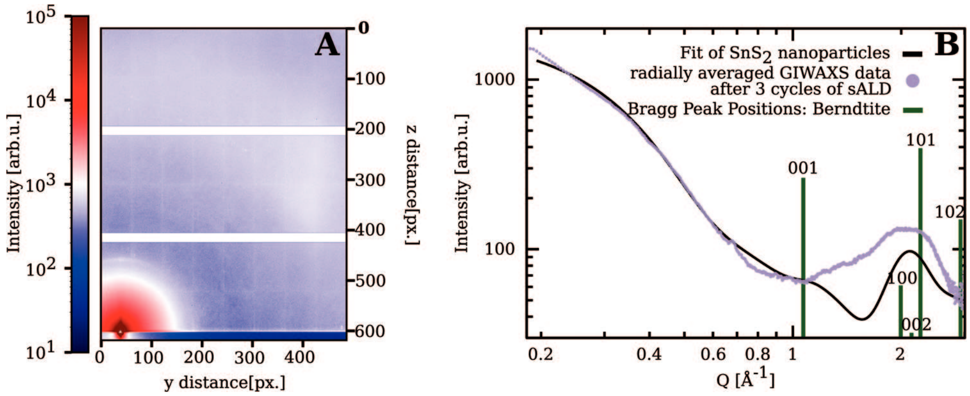

Figure 4. GIWAXS data of an MPTMS coated silicon wafer after 3 sALD cycles of SnS_2 coating. A) The 2D detector image is radially homogeneous and no preferred orientation of the deposited material can be observed. B) Radially averaged experimental data (violet circles), model fit (black line), and Bragg peak positions of berndtite with relative intensities (green lines).

upon further sALD cycles. This is probably due to active sites being lost in the cross linking during the second cycle. Therefore the remaining growth happens at remaining thiol groups or grain boundaries in the otherwise closed layer.

This continued growth is accompanied by slowly accumulating excess precursor that could not be effectively removed from the surface during the washing procedure. Therefore the island growth exceeds the growth rate of a single SnS_2 per cycle and an extended diffuse layer is formed which is observed by the large aggregates found in the AFM and EDX measurements.

3. Conclusion

In this work, a reproducible procedure to coat silicon wafers with a densely packed monolayer of MPTMS molecules is presented. This method produces layers with a low rate of polymer formation only. This way we were able to achieve a high surface coverage with thiol groups. These functional groups were used to seed nucleation of SnS_2 in a solution-based ALD procedure. We were able to resolve the nucleation process of SnS_2 on an MPTMS SAM during the first three cycles of an sALD procedure using X-ray reflectometry. In our comparison of ex situ and in situ measurements we found that SnS_2 forms a closed layer in the first two cycles and continues to grow in islands on the thiol functionalized silane SAMs. Furthermore, during the sALD procedure, SnS_2 is incorporated into the SAM which shows that in densely packed MPMTS layers the alkyl chains are free to move and therefore thiol groups are located on the surface as well as in the chain region. Subsequent coating cycles will continue the growth of the islands laterally and in height. This way during the first steps of the sALD process a closed SnS_2 layer is created, followed by the growth of SnS_2 islands, filling less than 50 % of the available space. These results are in good agreement with DFT calculations for the reaction kinetics of the first two half cycles of the coating procedure. and the nucleation behavior of SnS_2 on SiO_2 as observed during CVD.[27]

This growth behavior differs from the expected linear relation of coating cycles and layer thickness. However, the linear growth behavior in solution-based ALD is only observed for cycle numbers >10.[19,44,45] On the contrary, for low cycle numbers, growth rates not linearly dependent on cycle numbers have been observed. In these systems, the growth rates are highly dependent on the substrate surface.[45,46] In recent work Hilpert et al.[47] showed for the case of CuSCN on Si a growth behavior similar to our findings for SnS_2 on MPTMS: Materials forming nanoparticles on the substrate surface in the first few cycles before closing the gaps and becoming a filled layer. Furthermore, there are also other layer-by-layer processes that result in the formation of nanostructured surfaces.[48]

Therefore, our work represents a step toward a dedicated understanding of the formation processes of the very first layers in sALD and indicates the potential of sALD to become a simple and flexible alternative for ALD from the gas phase. Experimental difficulties of chemical bath deposition of excess precursors restricted our investigations to the analysis of the first two sALD cycles.

4. Experimental Section

Chemicals: For the functionalization of the wafers toluene (99.8 %, Sigma–Aldrich) and (3-Mercaptopropyl)trimethoxysilane (MPTMS) (95 %, Sigma–Aldrich) were used. The sALD procedure was performed in tetrahydrofuran (THF) (≥ 99.9 %, Sigma–Aldrich). Hydrogen sulfide dissolved in THF (0.8 M, Sigma–Aldrich) and Tetrakis(dimethylamido)tin (IV) (TDMASn) (99.9 %, Sigma–Aldrich) were used as precursors. The precursors were diluted with THF to a molar concentration of 1 mM. All chemicals were used as received. A compact overview over all chemicals used in this work is given in Table S1 (Supporting Information).

Silicon Wafers: All experiments in this work were performed on polished, {100}-oriented silicon wafers with native silicon oxide on the surface (Siltronics). The wafers were cut to dimensions 50 mm× 5 mm× 1 mm for use in the flow-through cell. Before use, the wafers were cleaned by sequential sonication in ethanol (99.97 %, Sigma–Aldrich), acetone (technical grade, Sigma–Aldrich), and toluene (99.8 %, Sigma–Aldrich). This was done in an inert Teflon vessel for 10 min at a time. The wafers were then dried with gaseous nitrogen. To remove further organic contaminants and to activate the surface, the wafers were cleaned for 1 h in a UV/ozone cleaner (Bioforce Nanoscience ProCleaner Plus). After activation the wafers were transferred with minimal contact to the environment into a glove box under nitrogen atmosphere for further treatment.

Self Assembled Monolayer (SAM) Preparation: The preparation of thiol functionalized SAMs was performed based on the work of Smith et al.[49] The wafers were coated in a 1 mM solution of MPTMS in anhydrous toluene at 70 °C, stirred at 300 rpm for 24 h under an inert nitrogen atmosphere in a glovebox (MBRAUN, Labmaster Pro DP). Afterward, the

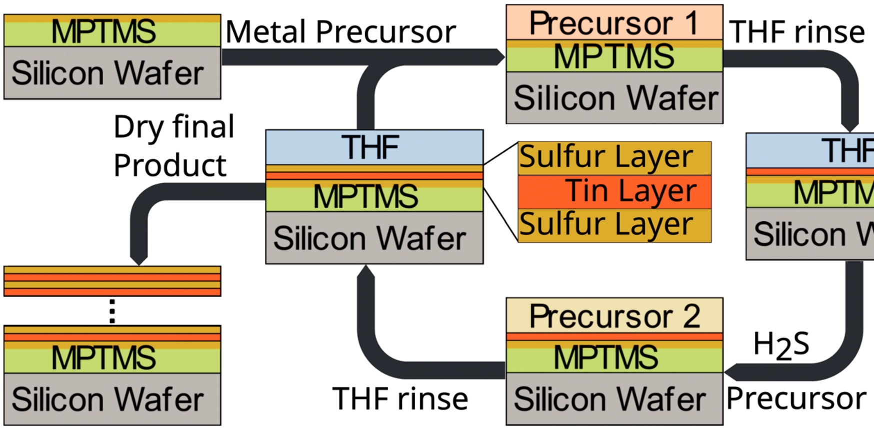

Figure 5. Schematic representation of the sALD procedure. As substrate a silicon wafer functionalized with an MPTMS SAM. In a repetitive procedure solutions of a metal precursor and H_2S are alternatingly brought into contact with the substrate. The precursors will react with the functional groups at the surface, introducing another type of functional groups for the subsequent precursor. After each precursor step the surface is cleaned with THF to remove remaining precursor and reactant molecules not bound to a functional group at the surface. This way every cycle will deposit one layer of material on the surface.

wafers were rinsed with toluene, sonicated again for 15 min in ethanol, acetone, and toluene, and dried at 110 °C in a vacuum drying oven (Binder, VDL23) for 15 min. Preparatory and post-processing cleaning steps were performed under a sterile class II safety cabinet (Thermo Scientific, KS 12).

Solution-Based Atomic Layer Deposition (sALD) Procedure: Details of the solution-based atomic layer deposition procedure are given in previous literature.[16–18] Silicon wafers functionalized with thiol terminated silane SAMs were used as substrates and alternatingly exposed to solutions of TDMASn and H_2S in a repetitive procedure.

In a first step a surplus of TDMASn reacted with the thiol groups present at the surface, binding the tin to the surface and producing dimethylamine:

$$\mathrm{R-SH + ((CH_3)_2N)_4Sn \longrightarrow R-S-Sn((CH_3)_2N)_3 + (CH_3)_2NH} \tag{2}$$

This reaction was self limiting due to the finite amount of thiol groups present at the surface. This step was followed by a washing step. The surface was rinsed with THF to remove all excess precursor molecules as well as reaction products not bound to the surface. This left the surface functionalized with dimethylamide groups.

In the next step H_2S was introduced to the surface. The dimethylamide groups reacted, forming free dimethylamine and thiol groups bound to the surface. This reaction was limited again by the amount of dimethylamide groups present:

$$\mathrm{R-S-Sn((CH_3)_2N)_3 + 3H_2S \longrightarrow R-S-Sn-(SH)_3 + 3(CH_3)_2NH} \tag{3}$$

The surface was then rinsed once more with THF to remove unbound material. In principle the growth of material, layer by layer, was therefore possible by continuously repeating these steps. The process is schematically presented in **Figure 5**.

Solution-Based Atomic Layer Deposition (sALD) Procedure—In Situ sALD Process: The sALD cycles were performed in a flow cell described in the work of Prihoda et al.[30] and under nitrogen atmosphere in a flow box provided by DESY. Great care was taken, that the substrate was not exposed to air or dried during the in situ experiments. First, the cell was filled with anhydrous THF. The THF volume in the cell was then replaced with a 1 mM TDMASn solution. The wafer was exposed to the precursor solution for 1 min. The cell was then flushed with 6 mL of THF, filled again with THF and kept for 3 min and flushed again with 6 mL of THF. The sALD half cycle was then repeated accordingly, this time using a 1 mM H_2S precursor solution. After each washing step, the cell was sealed and transferred from the flow box to the P08 beamline sample environment to perform a measurement. The substrate was submerged in THF during the measurement. The cell was flushed with the liquids using glas syringes. After the final in situ XRR measurement, the wafers were rinsed with THF and dried with dry nitrogen gas.

Laboratory XRR Measurements: Laboratory X-ray reflectivity(XRR) measurements were performed with a Rigaku SmartLab instrument at the Institute for Crystallography and Structural Physics (ICSP). X-rays were produced using a 9 kW rotating anode with a copper target at 45 kV and 160 mA, generating Cu-K_α radiation with a wavelength of 1.54 Å. The X-rays were monochromatized and parallelized with a goebel mirror in the so-called CBO unit, leading to a vertical divergence of 0.05 °. The horizontal divergence of the beam was fixed to 0.5 ° by the use of soller slits located in the beam path. A slit with a width of 10 mm was used to define the horizontal beam size. The beam height was confined to 0.1 mm. The same optical elements were placed behind the sample to minimize background and ensure the detection of the specularly reflected beam only. The sample was placed on a stage that allowed z movement and ϕ, χ, and ω rotation. Samples were aligned plane parallel to the beam path at 2θ-$\omega = 0$. The signal background was determined in a separate measurement. For this measurement the sample stage with the substrate was tilted in ω by 0.17 ° out of the specular reflection condition. The source and detector where moved to perform θ-2θ scans. A Hypix 3000 solid state 2D-detector was used as detector. Measurements were performed in 0D mode of the detector.

Synchrotron XRR Measurements: In situ XRR measurements were performed at the "High-Resolution Diffraction Beamline P08" at PETRA III (Deutsches Elektronen-Synchrotron DESY, Hamburg, Germany). The sample cell was mounted on the Kohzu six-circle diffractometer.[50] The X-ray wavelength was selected to be 0.496 Å. The direct beam was focused (1:1) to a cross-section of 80 × 250 μm^2 (vertical×horizontal). A collimation slit (6 mm × 1 mm, horizontal×vertical) for the reflection beam was installed at ≈30 mm from the sample, followed by a helium-inflated flight tube before the detector. A Pilatus 100k (172 × 172 μm^2 pixel size, Dectris AG, Switzerland) at 970 mm distance was used to detect the reflected beam. The reflected beam was calculated as the sum over a region of interest (ROI, 18 px × 18 px) around the direct beam position on the detector. The background was summed over a ROI of the same dimensions, shifted 50 px horizontally on the detector.

All measurements were performed in a flow cell of the design described in ref. [30] and filled with THF and helium, respectively. For the measurements the sample was first aligned plane-parallel to the direct beam and then the sample and detector where rotated to perform 2θ-ω measurements.

Data reduction: The XRR data were corrected for footprint effects of the incident beam at small angles assuming a rectangular beam and sample profiles with a sample size of 5 mm along the beam direction.[51] Data measured at P08 displayed a high sensitivity regarding minor tilts and dealignments of the sample during motor movements. This lead to shifts in the 2θ values. The 2θ values were therefore calibrated by fitting the position of the total reflection edge and Fresnel reflectivity.[52] The 2θ values were then corrected by a constant offset to shift the reflection edge at the position of the theoretical value. For this purpose custom Python fitting software based on the fitting algorithms in the package scipy was used. The resulting data was analyzed using GenX.[53] GenX uses the Parratt formalism[54] to simulate XRR data and a differential evolution[55] algorithm to fit the model to data.

Fit model: The layer model of Steinrück et al.[32,56] was used as a basis for the evaluation of the ex situ XRR curves. It describes the silicon wafer surface as three layers (silicon, electron depletion, silicon oxide). The MPTMS SAM on top of the wafer was also described by three layers (depletion layer, head group, tail group). This model had already been applied successfully by the group for the characterization of various interfacial phenomena on SAMs.[29,30]

The synchrotron XRR data was fitted with a multi layer model adapted from the previous model and refined with the ex situ measurements presented in Section S6 (Supporting Information). The model consists of an infinitely thick silicon substrate, two layers representing the silicon wafer interface (depletion layer, silicon oxide),[32] three layers for the MPTMS SAM (depletion, head group, carbon chain)[32,56] and THF as ambient medium. Additional layers were added between the THF phase and the MPTMS layer after each half cycle of the tin precursor, representing the deposition of material during the sALD process. The complete electron density profiles as well as a schematics of the fit model were visualized in Figure S1 (Supporting Information). Electron density difference profiles (EDDPs) of the MPTMS and sALD layers were calculated by subtracting the contributions of the silicon wafer, diffuse layer, and solvent.

Atomic Force Microscopy (AFM): AFM measurements were performed using an NX10 AFM from Park Systems.[57] Silicon cantilevers with an aluminum reflex coating (PPP-NCHR) were used.[58] They have a tip radius of <10 nm and typical force constants of $k \approx 42\ Nm^{-1}$with an eigenfrequency of $f \approx 330$ kHz. The Cantilevers were bought from NanoWorld and used as is. Each measurement was performed in non-contact mode with a set-point between 3 and 9 nm and a scan rate between 0.1 and 0.5 Hz. In each measurement a 10 µm × 10 µm surface was scanned. The measurements were performed on different, randomly chosen spots on each sample. From these measurements 2 µm × 2 µm areas were chosen to analyze the SnS_2 layer. Images were flattened and cropped. Line, region and grain analysis was performed on the images. All image processing and analysis steps were performed with the XE Image Processing Software from Park Systems.[59]

Contact Angle Measurements (CA): Contact angle measurements were conducted for all MPTMS coated Si wafers used as substrates for the sALD procedure. They were performed using a OCA-20 contact angle goniometer (DataPhysics Instruments GmbH).[60,61] Using 1 μL drops of ultrapure distilled water the contact angle was determined at six different spots on the surface using the sessile drop method. The values given are the arithmetic mean and the standard deviation of all measurements.

Grazing Incidence Wide-Angle X-Ray Scattering (GIWAXS): GIWAXS measurements were performed at the in-house versatile advanced X-ray scattering instrument erlangen (VAXSTER) at ICSP. The instrument was equipped with a liquid Gallium Metal Jet X-ray source from Excillum, Kista, Sweden, providing X-rays with a wavelength of 1.3414 Å. As detector a Pilatus 300K detector (500 Hz, 172 × 172 μm^2 pixel size) iwas used.

The GIWAXS measurements were performed with an incident X-ray beam of size 0.7mm × 0.7 mm at an incidence angle of $\alpha = 0.2\ ^\circ$ and a sample to detector distance of 167.32 mm. The whole beam path, the sample and the detector were kept in a vacuum below 10^{-5} bar during the experiments. The sample was placed on a sample stage that enabled movement in y- and z-direction as well as rotation around ϕ, χ, and α.

The 2D data was azimuthally averaged using the software fit2D.[62] GIWAXS data of a silicon wafer coated with a clean MPTMS monolayer was subtracted as background. The background data and experimental data before subtraction are displayed in Figure S3 (Supporting Information).

Density Functional Theory (DFT) Calculations: The DFT calculations were based on a series of geometry optimization runs, starting from initial arrangements suggested on an empirical basis using the Avogadro software.[63,64] Next, Gaussian 16[65] calculations were performed to identify minimum energy configurations first using the wB97X-D hybrid density functional which contained empirical dispersion corrections.[66] The relaxed structures were finally treated at the MP2 level using def2-TZVPP basis sets with triple-zeta valence quality and polarization functions.[67]

Supporting Information

Supporting Information is available from the Wiley Online Library or from the author.

Acknowledgements

The authors gratefully acknowledge the funding of the Federal Ministry of Education and Research of Germany (BMBF) in the framework of project No. 05K16WE1 and the research unit FOR 1878 'Functional Molecular Structures on Complex Oxide Surfaces'.

The authors acknowledge the financial support by the consortium DAPHNE4NFDI in the context of the NFDI e.V. The consortium is funded by DFG (project number 460248799).

The authors acknowledge DESY (Hamburg, Germany), a member of the Helmholtz Association HGF, for the provision of experimental facilities. Parts of this research were carried out at PETRA III and the authors would like to thank Dr. Florian Bertram and Mr. René Kirchhof for assistance in using P08. Additionally the authors want to thank Dr. Milena Lippmann and Mrs. Brit Heilmann for their supervision and help in using the chemistry labs. Beamtime was allocated for proposal I-20180247. K.G., A.P., and T.U. acknowledge the financial support of FAU EAM / CENEM. S.P. and D.Z. gratefully acknowledge funding from the Deutsche Forschungsgemeinschaft via grant no. ZA 420/15-1.

The authors would also like to thank Prof. Dr. Reinhard Neder for his help in operating the DISCUS suite.

Conflict of Interest

The authors declare no conflict of interest.

Author Contributions

K.G. and A.P. contributed equally to the article. A.P. performed the characterization of the MPTMS-SAM and ex situ experiments of the sALD procedure. A.P. wrote the sections about the respective experiments and contributed parts of the MPTMS SAM preparation, sALD process, and contact angle measurements. K.G. planned and performed the in situ measurements and further characterization experiments. K.G. composed the draft of this work. K.G., A.P., and T.U. designed the concept of this study. C.S., A.P., and J.D. assisted in performing the experiments at P08 at DESY and treating the acquired data. M.D. performed the EDX measurements and helped with the interpretation. S.P. performed the DFT calculations. S.P. and D.Z. helped with the interpretation of the DFT results. All authors contributed to the revision of the manuscript.

Data Availability Statement

Data is published on zenodo.org under zenodo.12633113.

Keywords

AFM, GIWAXS, SAM, sALD, solution atomic layer deposition, XRR

Received: November 24, 2023
Revised: June 4, 2024
Published online: July 31, 2024

---

[1] A. K. Geim, *Science (New York, N.Y.)* **2009**, *324*, 1530.

[2] A. N. Grigorenko, M. Polini, K. S. Novoselov, *Nat. Photonics* **2012**, *6*, 749.

[3] X. Li, J. Yu, S. Wageh, A. A. Al-Ghamdi, J. Xie, *Small* **2016**, *12*, 6640.

[4] M. Long, P. Wang, H. Fang, W. Hu, *Adv. Funct. Mater.* **2019**, *29*, 1803807.

[5] T. Tan, X. Jiang, C. Wang, B. Yao, H. Zhang, *Adv. Sci.* **2020**, *7*, 2000058.

[6] G. Tang, P. You, Q. Tai, A. Yang, J. Cao, F. Zheng, Z. Zhou, J. Zhao, P. K. L. Chan, F. Yan, *Adv. Mater.* **2019**, *31*, 1807689.

[7] Z.-L. Lei, B. Guo, *Adv. Sci.* **2022**, *9*, 2102924.

[8] S. Kang, D. Lee, J. Kim, A. Capasso, H. S. Kang, J.-W. Park, C.-H. Lee, G.-H. Lee, *2D Mater.* **2020**, *7*, 022003.

[9] V. Cremers, R. L. Puurunen, J. Dendooven, *Appl. Phys. Rev.* **2019**, *6*, 021302.

[10] P. O. Oviroh, R. Akbarzadeh, D. Pan, R. A. M. Coetzee, T.-C. Jen, *Sci. Technol. Adv. Mater.* **2019**, *20*, 465.

[11] N. E. Richey, C. de Paula, S. F. Bent, *J. Chem. Phys.* **2020**, *152*, 040902.

[12] J. A. Raiford, S. T. Oyakhire, S. F. Bent, *Energy Environ. Sci.* **2020**, *13*, 1997.

[13] N. Lee, G. Lee, H. Choi, H. Park, Y. Choi, K. Kim, Y. Choi, J.-W. Kim, H. Yuk, O. Sul, S.-B. Lee, H. Jeon, *Appl. Surf. Sci.* **2019**, *496*, 143689.

[14] G. C. Correa, B. Bao, N. C. Strandwitz, *ACS Appl. Mater. Interfaces* **2015**, *7*, 14816.

[15] N. Lee, H. Choi, H. Park, Y. Choi, H. Yuk, J. Lee, H. Jeon, *Nanotechnology* **2020**, *31*, 265604.

[16] M. K. S. Barr, J. Bachmann, B Zhao, P. V. Grundherr, M. H. Uddin, V. Koch, M. Halik, *ECS Meeting Abstracts* **2021**, *MA2021-02*, 884.

[17] J. Fichtner, Y. Wu, J. Hitzenberger, T. Drewello, J. Bachmann, *ECS J. Solid State Sci. Technol.* **2017**, *6*, N171.

[18] V. M. Koch, M. K. S. Barr, P. Büttner, I. Mínguez-Bacho, D. Döhler, B. Winzer, E. Reinhardt, D. Segets, J. Bachmann, *J. Mater. Chem. A* **2019**, *7*, 25112.

[19] Y. Cao, S. Zhu, J. Bachmann, *Dalton Trans.* **2021**, *50*, 13066.

[20] K. Sharma, S. Patial, P. Singh, A. A. P. Khan, V. Saini, A. K. Nadda, C. M. Hussain, V.-H. Nguyen, C. C. Nguyen, T. B. H. Nguyen, S. Y. Kim, Q. v. Le, P. Raizada, *Sol. Energy* **2022**, *231*, 546.

[21] G. Li, R. Su, J. Rao, J. Wu, P. Rudolf, G. R. Blake, R. A. de Groot, F. Besenbacher, T. T. M. Palstra, *J. Mater. Chem. A* **2016**, *4*, 209.

[22] J. Yu, C.-Y. Xu, F.-X. Ma, S.-P. Hu, Y.-W. Zhang, L. Zhen, *ACS Appl. Mater. Interfaces* **2014**, *6*, 22370.

[23] L. Chen, E. Liu, F. Teng, T. Zhang, J. Feng, Y. Kou, Q. Sun, J. Fan, X. Hu, H. Miao, *Appl. Surf. Sci.* **2019**, *467-468*, 698.

[24] X. Guo, F. Zhang, Y. Zhang, J. Hu, *J. Mater. Chem. A* **2023**, *11*, 7331.

[25] W. Hu, T. T. Hien, D. Kim, H. S. Chang, *Nanomaterials* **2019**, *9*, 1083.

[26] J. Xia, D. Zhu, L. Wang, B. Huang, X. Huang, X.-M. Meng, *Adv. Funct. Mater.* **2015**, *25*, 4255.

[27] H. Zhang, T. van Pelt, A. N. Mehta, H. Bender, I. Radu, M. Caymax, W. Vandervorst, A. Delabie, *2D Mater.* **2018**, *5*, 035006.

[28] J. E. Wittmann, L. M. S. Stiegler, C. Henkel, J. Träg, K. Götz, T. Unruh, D. Zahn, A. Hirsch, D. Guldi, M. Halik, *Adv. Mater. Interfaces* **2019**, *6*, 1801930.

[29] K. Götz, I. Stollberg, A. Prihoda, F. Bertram, E. Metwalli, T. Zech, T. Unruh, *Surf. Sci.* **2022**, *721*, 122066.

[30] A. Prihoda, J. Will, P. Duchstein, B. Becit, F. Lossin, T. Schindler, M. Berlinghof, H.-G. Steinrück, F. Bertram, D. Zahn, T. Unruh, *Langmuir: The ACS J. Surf. and Colloids* **2020**, *36*, 12077.

[31] Y. Cao, T. Wähler, H. Park, J. Will, A. Prihoda, N. Moses Badlyan, L. Fromm, T. Yokosawa, B. Wang, D. M. Guldi, A. Görling, J. Maultzsch, T. Unruh, E. Spiecker, M. Halik, J. Libuda, J. Bachmann, *Adv. Mater. Interfaces* **2020**, *7*, 2001493.

[32] H.-G. Steinrück, A. Schiener, T. Schindler, J. Will, A. Magerl, O. Konovalov, G. Li Destri, O. H. Seeck, M. Mezger, J. Haddad, M. Deutsch, A. Checco, B. M. Ocko, *ACS Nano* **2014**, *8*, 12676.

[33] D. Rébiscoul, V. Perrut, T. Morel, C. Jayet, R. Cubitt, P.-H. Haumesser, *Langmuir: The ACS J. Surf. and Colloids* **2010**, *26*, 8981.

[34] MSDSNo. *907/2006 [Online]. Sigma-Aldrich: St. Louis, Missouri, October 19, 2022*, https://www.sigmaaldrich.com/DE/de/sds/aldrich/175617 (accessed: December 2023), *3-Mercaptopropyltrimethoxysilan*.

[35] M. Hu, S. Noda, T. Okubo, Y. Yamaguchi, H. Komiyama, *Appl. Surf. Sci.* **2001**, *181*, 307.

[36] M. Ben Haddada, J. Blanchard, S. Casale, J.-M. Krafft, A. Vallée, C. Méthivier, S. Boujday, *Gold Bulletin* **2013**, *46*, 335.

[37] Z. JIANG, X. CHENG, *J. Rare Earth.* **2009**, *27*, 490.

[38] X. CHENG, *Ind. Lubr.Tribology* **2009**, *61*, 27.

[39] K. Viswanathan, H. Ozhalici, C. L. Elkins, C. Heisey, T. C. Ward, T. E. Long, *Langmuir* **2006**, *22*, 1099.

[40] P. Virtanen, R. Gommers, T. E. Oliphant, M. Haberland, T. Reddy, D. Cournapeau, E. Burovski, P. Peterson, W. Weckesser, J. Bright, S. J. van der Walt, M. Brett, J. Wilson, K. J. Millman, N. Mayorov, A. R. J. Nelson, E. Jones, R. Kern, E. Larson, C. J. Carey, İ. Polat, Y. Feng, E. W. Moore, J. VanderPlas, D. Laxalde, J. Perktold, R. Cimrman, I. Henriksen, E. A. Quintero, C. R. Harris, et al., *Nat. Methods* **2020**, *17*, 261.

[41] Y. Wu, D. Döhler, M. Barr, E. Oks, M. Wolf, L. Santinacci, J. Bachmann, *Nano Lett.* **2015**, *15*, 6379.

[42] R. M. Hazen, L. W. Finger, *Am. Mineral.* **1978**, *63*, 289.

[43] T. Proffen, R. B. Neder, *J. Appl. Crystallogr.* **1997**, *30*, 171.

[44] M. K. S. Barr, S. Nadiri, D.-H. Chen, P. G. Weidler, S. Bochmann, H. Baumgart, J. Bachmann, E. Redel, *Chem. Mater.* **2022**, *34*, 9836.

[45] V. M. Koch, J. Charvot, Y. Cao, C. Hartmann, R. G. Wilks, I. Kundrata, I. Mínguez-Bacho, N. Gheshlaghi, F. Hoga, T. Stubhan, W. Alex, D. Pokorný, E. Topraksal, A.-S. Smith, C. J. Brabec, M. Bär, D. M. Guldi, M. K. S. Barr, F. Bureš, J. Bachmann, *Chem. Mater.* **2022**, *34*, 9392.

[46] V. M. Koch, M. K. S. Barr, P. Büttner, I. Mínguez-Bacho, D. Döhler, B. Winzer, E. Reinhardt, D. Segets, J. Bachmann, *J. Mater. Chem. A* **2019**, *7*, 25112.

[47] F. Hilpert, P.-C. Liao, E. Franz, V. M. Koch, L. Fromm, E. Topraksal, A. Görling, A.-S. A. Smith, M. K. S. Barr, J. Bachmann, O. Brummel, J. Libuda, *ACS Appl. Mater. Interfaces* **2023**, *15*, 19536.

[48] D. Steinbach, R. Neubert, S. Gersdorf, C. Schimpf, D. Erb, D. Rafaja, F. A. Plamper, F. Mertens, *CrystEngComm* **2023**, *25*, 4568.

[49] E. A. Smith, W. Chen, *Langmuir: The ACS journal of surfaces and colloids* **2008**, *24*, 12405.

[50] O. H. Seeck, C. Deiter, K. Pflaum, F. Bertam, A. Beerlink, H. Franz, J. Horbach, H. Schulte-Schrepping, B. M. Murphy, M. Greve, O. Magnussen, *J. Synchrotron Radiat.* **2012**, *19*, 30.

[51] A. Gibaud, G. Vignaud, S. K. Sinha, *Acta Cryst. Section A Foundations of Crystallography* **1993**, *49*, 642.

[52] A. Gibaud, S. Hazra, *Curr. Sci.* **2000**, *78*, 1467.

[53] A. Glavic, M. Björck, *J. Appl. Crystallogr.* **2022**, *55*, 1063.

[54] L. G. Parratt, *Phys. Rev.* **1954**, *95*, 359.

[55] M. Björck, *J. Appl. Crystallogr.* **2011**, *44*, 1198.

[56] H.-G. Steinrück, J. Will, A. Magerl, B. M. Ocko, *Langmuir: The ACS journal of surfaces and colloids* **2015**, *31*, 11774.

[57] *Park nx10 - specifications | park atomic force microscope*, https://www.parksystems.com/products/small-sample-afm/park-nx10/specifications (accessed: July 2023).

[58] *Nchr-nanoworld®*, https://www.nanoworld.com/pointprobe-tapping-mode-reflex-coated-afm-tip-nchr (accessed: July 2023).

[59] *Xei powerful image processing tool for spm data*, https://cores.research.asu.edu/sites/default/files/2020-08/XEIManual_1_8_0_0.pdf (accessed: August 2023).
[60] *Oca optical contact angle measuring and contour analysis systems - dataphysics instruments*, https://www.dataphysics-instruments.com/products/oca/ (accessed: August 2023).
[61] *Oca product series*, https://www.dataphysics-instruments.com/Downloads/OCA_EN.pdf?v=1.8 (accessed: August 2023).
[62] A. P. Hammersley, *J. Appl. Crystallogr.* **2016**, *49*, 646.
[63] *Avogadro: an open-source molecular builder and visualization tool*, (accessed: August 2023).
[64] M. D. Hanwell, D. E. Curtis, D. C. Lonie, T. Vandermeersch, E. Zurek, G. R. Hutchison, *J. Cheminf.* **2012**, *4*, 17.
[65] *Gaussian 16, Revision A. 03, Gaussian, Inc., Wallingford CT*, **2016**.
[66] J.-D. Chai, M. Head-Gordon, *Phys. Chem. Chem. Phys.* **2008**, *10*, 6615.
[67] F. Weigend, R. Ahlrichs, *Phys. Chem. Chem. Phys.* **2005**, *7*, 3297.